Article

Quantification of Aquarius, SMAP, SMOS and Argo-Based Gridded Sea Surface Salinity Product Sampling Errors

Séverine Fournier [1,*], Frederick M. Bingham [2], Cristina González-Haro [3], Akiko Hayashi [1], Karly M. Ulfsax Carlin [4], Susannah K. Brodnitz [2], Verónica González-Gambau [3] and Mikael Kuusela [5]

1 Jet Propulsion Laboratory, California Institute of Technology, Pasadena, CA 91109, USA
2 Center for Marine Science, University of North Carolina Wilmington, Wilmington, NC 28403, USA
3 Department of Physical Oceanography, Institute of Marine Sciences, CSIC, Barcelona Expert Center, ES08003 Barcelona, Spain
4 Catlin Engineers & Scientists, Wilmington, NC 28405, USA
5 Department of Statistics and Data Science, Carnegie Mellon University, Pittsburgh, PA 15213, USA
* Correspondence: severine.fournier@jpl.nasa.gov

Abstract: Evaluating and validating satellite sea surface salinity (SSS) measurements is fundamental. There are two types of errors in satellite SSS: measurement error due to the instrument's inaccuracy and problems in retrieval, and sampling error due to unrepresentativeness in the way that the sea surface is sampled in time and space by the instrument. In this study, we focus on sampling errors, which impact both satellite and in situ products. We estimate the sampling errors of Level 3 satellite SSS products from Aquarius, SMOS and SMAP, and in situ gridded products. To do that, we use simulated L2 and L3 Aquarius, SMAP and SMOS SSS data, individual Argo observations and gridded Argo products derived from a 12-month high-resolution 1/48° ocean model. The use of the simulated data allows us to quantify the sampling error and eliminate the measurement error. We found that the sampling errors are high in regions of high SSS variability and are globally about 0.02/0.03 psu at weekly time scales and 0.01/0.02 psu at monthly time scales for satellite products. The in situ-based product sampling error is significantly higher than that of the three satellite products at monthly scales (0.085 psu) indicating the need to be cautious when using in situ-based gridded products to validate satellite products. Similar results are found using a Correlated Triple Collocation method that quantifies the standard deviation of products' errors acquired with different instruments. By improving our understanding and quantifying the effect of sampling errors on satellite-in situ SSS consistency over various spatial and temporal scales, this study will help to improve the validation of SSS, the robustness of scientific applications and the design of future salinity missions.

Keywords: sea surface salinity; SMAP; SMOS; Aquarius; sampling errors

1. Introduction

Sea surface salinity (SSS) has been observed using satellites since 2010 with the launch of the European Space Agency (ESA) Soil Moisture and Ocean Salinity (SMOS) mission [1,2], followed by the launches of the National Aeronautics and Space Administration (NASA)/SAC-D Aquarius [3] and Soil Moisture Active Passive (SMAP) [4] missions in 2011 and 2015, respectively. The three missions provide synoptic measurements of SSS over the global ocean. Satellite measurements of SSS have been applied to a broad range of scientific research studies including ocean dynamics, climate variability, Earth's water and carbon cycles, and marine biogeochemistry ([5], and references therein). Evaluating and validating satellite SSS measurements is therefore fundamental for scientific applications and future satellite mission designs, and it is of extreme importance to understand and quantify the error budget, in particular the error associated with the validation process of satellite SSS measurements.

The most widely used type of satellite product for studying SSS are gridded, level 3 (L3) or 4 (L4), products. These are formulated by averaging or optimally interpolating swath-based L2 satellite values (plus in situ measurements or model output in the case of an L4 product) onto a regular grid [6–8]. These L3 or L4 products are convenient to use for studying SSS as they come packaged in a regular time/space grid for easy display and analysis. Such products can be found in quasi-weekly or monthly versions, e.g., [9]. Similarly, in situ measurements are often combined into gridded products, two common ones being the Scripps Institution of Oceanography (SIO) [10] and EN4 versions [11]. Due to the sparser nature of in situ sampling relative to satellites, these are usually monthly on a $1° \times 1°$ grid.

There are two types of errors in satellite observations of SSS, measurement error and sampling error. Measurement errors are those associated with the observation itself, such as instrumental errors, and problems in the retrieval process [8,12]. Sampling errors are due to the unrepresentativeness of the instrument. While satellite SSS measurement errors are much larger than those of in situ data such as Argo floats (~0.2 psu for satellite versus +/− 0.01 psu for in situ [13]), both in situ and satellite gridded products are subject to sampling errors. The salinity value at one grid point of an Argo gridded monthly product has been computed using in situ measurements available during that period of time within that pixel, combined using some statistically optimal algorithm. However, in situ measurements being sparse in time and space, some salinity signals are not captured by this in situ sampling, introducing both potential time and space aliasing into the product. Similarly, weekly and monthly L3 satellite SSS gridded products are computed by averaging all the L2 SSS data available over the given period of time within the grid cell. However, because of the satellite repeat cycle, each region of the world is sampled only about every 3–7 days; therefore, some high frequency salinity features are not captured by satellites. We call this temporal aliasing. Additionally, each L2 SSS value is computed by doing a weighted average over the satellite footprint (60 to 150 km), within which there is some variability. This sub-footprint variability is therefore not captured by the satellite [14–17]. We call this spatial aliasing.

Satellite L3 SSS products are widely evaluated against Argo monthly gridded salinity products or model or reanalysis output, e.g., [12], which have their own sampling errors. Ref. [18] demonstrates that the consistency between monthly Aquarius and monthly gridded Argo near surface salinity is comparable to the consistency between two different monthly gridded Argo-based products in the Tropics and mid-latitudes. In situ sampling error is part of the difference in the consistency between Argo gridded products. The sampling errors in gridded in situ products complicate the validation process of satellite SSS products. Therefore, the sampling errors associated with the Argo gridded products need to be assessed along with satellite products and this has not been investigated yet.

Previous studies have explored satellite sampling errors. Ref. [5], based on the work of [16,19] showed that sampling errors of monthly satellite fields are large near the outflows of major rivers (e.g., Amazon, Congo, Bay of Bengal), western boundary currents, and several other coastal regions where salinity is highly variable. They can reach 0.7 psu in the vicinity of the Amazon River, 0.5 psu along the Gulf Stream, 0.4 psu in the Bay of Bengal, and above 1 psu in extreme cases, such as in the Gulf Stream region. Ref. [20] used tropical mooring data to describe high-frequency SSS variability in the tropical ocean. They found that over 10-day-long records, standard deviation values were about 0.1 psu, in some instances exceeded 0.2 psu, and were driven mostly by precipitation. Ref. [21], in the first global assessment of its kind, showed that Aquarius salinity retrievals can misrepresent true monthly averages due to their low temporal resolution (weekly) compared to models, which generally have higher temporal resolution (hourly to daily) and allow the production of robust monthly mean average fields. They show that in monthly mean maps, the Aquarius SSS temporal aliasing error is about 0.02 psu on average and above 0.1 psu in regions with enhanced high frequency SSS variability such as coastal areas. However, this

work was performed using a model that had relatively low (1/12°) resolution compared to currently available models.

Previous studies using in situ measurements to investigate these issues have been complicated by the fact that the satellite sampling error, the satellite measurement error and the in situ sampling error get entangled. In this work, we use a 12-month high-resolution (HR) 1/48° ocean model to investigate the sampling errors of both satellite and in situ gridded SSS products. We are interested in quantifying the sampling error only and the model is an excellent tool to disentangle the measurement error from the sampling error by freeing ourselves from the measurement error. By considering the model as our ground truth, no measurement error remains and by sampling the model in the same manner as the satellites and in situ instruments sample the ocean, we can simulate the validation process and quantify the sampling errors.

2. Materials and Methods

Our analysis is carried out starting from Level 2 (L2) satellite SSS from Aquarius, SMAP and SMOS, Argo single point measurements and a high-resolution ocean model. A brief description of the datasets is provided in this section. The method used to simulate the L2 Aquarius and SMAP SSS data and the Argo single point measurements from the model is based on [17]. A brief description is provided below but more details can be found in that reference. However, we provide below a detailed description of the method to simulate L2 SMOS from the model as well as the method to compute the gridded L3 Aquarius, SMAP, SMOS SSS, and Argo-based gridded products from the model, which extends the work of [17].

2.1. Observations

We use the L2 version 5 Aquarius SSS product and in particular the coordinates (latitudes and longitudes) and times of measurement. This product consists of footprints for the beams whose sizes are 76 km (along-track) × 94 km (cross-track), 84 km × 120 km, and 96 km × 156 km, yielding a total cross-track swath of 370 km. This product is distributed by the Physical Oceanography Distributed Active Archive Center (PO.DAAC). L2 Aquarius SSS data are available from the end of August 2011 to early June 2015 (https://doi.org/10.5067/AQR50-2SOCS; accessed on 1 March 2020).

SMAP SSS observations have a resolution of 40 km [12], which is approximately two times better than that of Aquarius (approximately 150 km) and is less affected by Radio Frequency Interference (RFI) in the coastal oceans than ESA's SMOS mission. We use the L2 40 km version 4.0 SMAP SSS produced by Remote Sensing Systems (RSS) [22] sampled on a 1/4° grid. These L2 data are L-band radiometer-based and are publicly available at the PO.DAAC. The footprint sizes are 39 km (along-track) × 47 km (cross-track), approximated as a 40 km circle [17]. SMAP SSS data are available starting from April 2015 (https://doi.org/10.5067/SMP3A-2SOCS; accessed on 1 March 2020).

We also use the L2 v700 SMOS SSS product produced and distributed by ESA. The data are available through the ESA SMOS Online Dissemination Service (https://smos-diss.eo.esa.int/oads/access/collection/SMOS_Open_V7 (accessed on 1 March 2020)). The tracks are provided daily from January 2010 to present. The footprint is 35 km (nadir) to 65 km (at maximum incidence angle).

We also used the Argo floats positions from the International Argo Program between November 2011 and October 2012. The data were obtained from the National Oceanographic Data Center (NODC), now the National Centers for Environmental Information (NCEI). There was no additional quality control performed, but we only selected measurements with a quality control flag of "good", with a topmost measurement above 10 m depth.

2.2. Model

Our proposed study is taking advantage of a ground-breaking state-of-the-art high-resolution ocean model implemented as a collaborative effort of the ocean modeling teams at MIT and JPL. The MITgcm [23] with a Latitude–Longitude polar Cap (LLC) numerical grid [24] is used. The nominal horizontal grid spacing is 1/48° and 90 vertical levels in z-coordinates. The period of simulation spans from 13 September 2011 to 15 November 2012, but we used one year of model output, 1 November 2011–31 October 2012. The three-dimensional model prognostic variables were saved every hour. The model has been validated in terms of balanced motions and the internal gravity wave continuum [25–29]. This model is the highest-resolution global ocean simulation available at the present time. It has tidal-forcing, so it reproduces the most realistic internal gravity wave continuum [30].

2.3. Method

2.3.1. Level 2 and 3 Aquarius and SMAP Simulations

The first step in our study is to simulate Aquarius and SMAP L2 and then L3 SSS data using the model. For that we followed the method used in [17]. We take as our initial observations the ground tracks of the Aquarius and SMAP satellites for the model period, provided in the L2 product files. Regarding SMAP, as the satellite time period (2015-onward) does not coincide with the model period (2011–2012), so we use the 2016–2017 SMAP ground tracks but subtract 5 years from the observation dates. Simulated Aquarius and SMAP L2 observations are generated by convolving model observations under the satellite ground tracks with the satellite antenna pattern out to a radius more or less equal to the footprint size. We create a simulated L2 observation at the closest hourly model time step from each L2 Aquarius and SMAP observation. We compute a Gaussian-weighted average of all the model SSS data that fall under the satellite footprint (100 km for Aquarius and 47 km for SMAP):

$$Simulated\ SSS_{L2} = \sum_i \frac{w_i SSS_i}{\sum_i wi} \tag{1}$$

$$with\ w_i = e^{-\ln(2)\left(\frac{r_i}{r_0}\right)^2} \tag{2}$$

With r the distance of each model value from the L2 observation; $r_0 = d_0/2$ with d_0 the half-power footprint size (40 km for SMAP and 100 km for Aquarius). Further details on the method to simulate SMAP and Aquarius L2 data are explained in [17].

Simulated Aquarius and SMAP L3 fields are then generated by smoothing or averaging the simulated L2 data as is performed currently to produce the L3 fields. For SMAP, as the L2 data are sampled on a regular 1/4° grid, in order to obtain the L3 data, a time average at each grid cell (8-day or monthly) is performed. For Aquarius, to obtain L3 data, we find the L2 SSS data around each L3 1° grid cell, within 100 km radius and a smoothing of these L2 data is performed using a local polynomial fitting over 7 days or a month. More details can be found in the official documentation (https://podaac-tools.jpl.nasa.gov/drive/files/allData/aquarius/docs/v2/AquariusLevel3_GriddingSmoothingPaper_Lilly&Lagerloef2008.pdf (accessed on 1 March 2020)). Note, the Aquarius L3 simulation data are computed on a 1° × 1° grid, whereas the SMAP (and SMOS) simulation data are on a 1/4° × 1/4° grid.

2.3.2. Level 2 and 3 SMOS Simulations

The simulation of SMOS L2 SSS data is more complex than for Aquarius and SMAP as SMOS uses an interferometric radiometer. While the SMOS swath is about 1300 km wide, we only take into account the data within 314 km on either side of nadir, the alias free field of view. At each incidence angle (provided in the L2 files), the footprint varies, being 35 km at nadir and 62 km at 314 km from nadir. We then proceed as we did for Aquarius and SMAP at each incidence angle by computing a Gaussian-weighted average of the model SSS over the varying size of the footprint (see Equations (1) and (2)). To compute the simulated L3 SMOS SSS, the simulated L2 values within 9 days are averaged

over each grid cell (1/4° grid), applying a weight that depends on the radiometric accuracy (RA), theoretically computed as in [31]. Figure 1 provides the radiometric accuracy in Kelvin (K) for a finite number of distances from nadir. For each L2 SSS value simulated, we compute an associated RA by simply linearly interpolating the values in Figure 1 to the actual distance from the nadir provided in the SMOS L2 dataset. The SMOS L3 SSS value at the grid cell *i* is calculated as the sum of all the weighted L2 SSS values (*j*) that fall in the grid cell *i*:

$$SSS_i = \sum_j w_j SSS_j \tag{3}$$
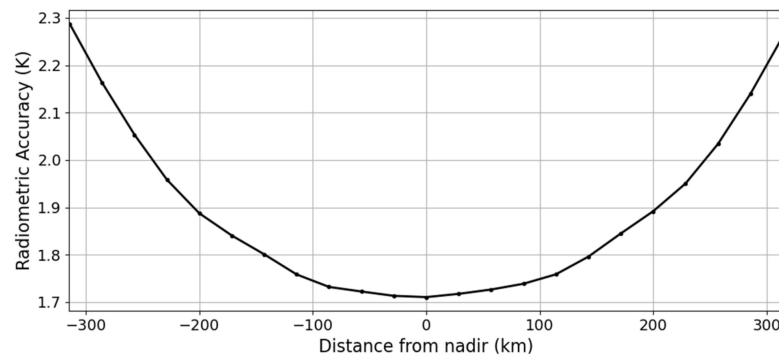
Figure 1. Radiometric accuracy coefficients as a function of distance from nadir from [31] used to compute the simulated L3 SMOS SSS data.

With the weight for each L2 value that falls in the grid cell *i* calculated as:

$$w_j = \frac{1}{RA_j^2 \sum_k \frac{1}{RA_k^2}} \tag{4}$$

With *k* looping all the *j* in the L3 grid cell *i*.

2.3.3. Argo Single Float and Gridded Products Simulations

For the in situ data, the model is sampled at individual locations using the Argo position information, see [17]. We take as our initial observations the simulated SSS values at the locations of Argo float observations for the model period. The simulated individual Argo data is then used to generate monthly 1° × 1°-grid fields for the model period in the same manner as [10]. This product has been widely used for scientific applications and for evaluating satellite SSS. The documentation and codes used to compute the Argo-based gridded product are based on the reproduction of the Roemmich and Gilson maps in [32], and available at https://github.com/mkuusela/ArgoMappingPaper (accessed on 1 March 2020). The [32] program to make a gridded product uses residuals, i.e., salinity values minus monthly mean fields. Since we only had one year of model data instead of the many years that the [10] product gets its strength from, we used a two-iteration approach to approximate a mean field from just one year of model data. A similar iterative approach was also used and justified in [33]. For the first iteration we used the mean field from real world [10] data, and computed residuals by subtracting the mean field from the simulated salinity value, by month of observation and nearest neighbor in space. Running the residuals through [32]'s reproduction of the Roemmich and Gilson mapping algorithm resulted in gridded simulated anomalies, which were then added back to the monthly mean fields to obtain simulated gridded salinity values. For the second iteration, we averaged all the initial simulated anomalies for the full year. We assumed that the nonzero values expressed systematic differences between the model's actual mean field and the mean field we initially used, from real-world data. We added the year average simulated anomalies to the initial monthly mean fields to get updated monthly mean fields, and calculated residuals in the same manner as before. We then ran these residuals through [32]'s program

and added the output anomalies back to the second iteration mean fields for the final simulated gridded salinity values.

2.3.4. Model Fields

We also produce "ground truth" L3 fields by averaging the model over quasi-weekly (7 days to compare with Aquarius, 8 days to compare with SMAP and 9 days to compare with SMOS) and monthly periods to compare with Aquarius, SMAP, SMOS and Argo-based grids, within grid cells at 0.25° resolution (to compare with SMAP and SMOS) and at 1° resolution to compare with Aquarius and the Argo gridded products.

To summarize, with these initial steps, we have generated a set of simulated (1) individual pointwise in situ observations, (2) ground truth fields at 0.25° (monthly and quasi-weekly) and 1° (monthly) resolution, (3) L2 satellite observations for three different satellites, (4) quasi-weekly and monthly L3 satellite fields for three different satellites, and (5) monthly gridded Argo products. All of the aforementioned (except the ground truth fields) are taken from the model using the L2 ground tracks and Argo sample positions as the initial input. Figure 2a shows the August 2012 ECCO (ground truth) SSS. Maps of the simulated L3 Aquarius, SMAP, SMOS and Argo-based gridded SSS for that month (not shown here) are very similar to the ECCO map. Figure 2 also shows the 1-year standard deviation of monthly SSS from the ground truth (ECCO) and the simulated Aquarius, SMAP, SMOS and Argo-based L3 products. We can see that while the amplitude of the variability differs slightly from one product to another, regions of high SSS variability are generally similar in all products. The simulated Argo-based product shows less variability than the simulated satellite products in the Tropical Pacific and Indian Ocean. The SSS standard deviation over 1 year is over 0.8 psu at various river mouths, and in the Gulf Stream, eastern Pacific fresh pool, Maritime Continent, and InterTropical Convergence Zone (ITCZ) for SMOS, Aquarius, SMAP and Argo gridded products. The Argo simulated product does show more variability near the Amazon River mouth compared to the simulated satellite product. This is probably due to the fact that we used the mean field from real world [10] data to compute the simulated Argo gridded product from the simulated single point Argo floats and the ECCO model is not forced by interannual river discharge observation causing SSS near river mouths to not be very well represented.
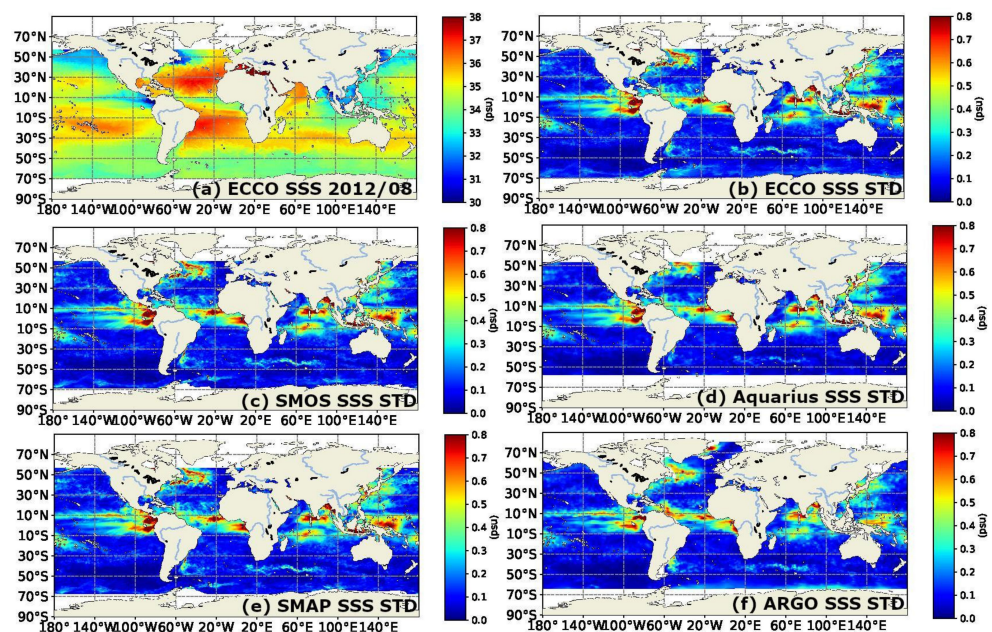

Figure 2. (**a**) August 2012 map of ECCO (1/48°) SSS, and maps of 1 year (November 2011–October 2012) standard deviation of monthly SSS (**b**) from ECCO and for the simulated L3 (**c**) SMOS (0.25°), (**d**) Aquarius (1°), (**e**) SMAP (0.25°) and (**f**) Argo-based (1°) gridded SSS.

3. Results

The simulated satellite and in situ data are used to quantify the sampling errors of the Aquarius, SMAP and SMOS satellites at L3 as well as the Argo-based gridded product. We first compare the simulated satellite and Argo-based products with the model at weekly and monthly scales (Figures 3 and 4) at their respective spatial resolutions in order to get an overview of the patterns of the satellite and in situ sampling errors. For that, we compute the absolute mean, and standard deviation of the differences between satellite/in situ and the model.
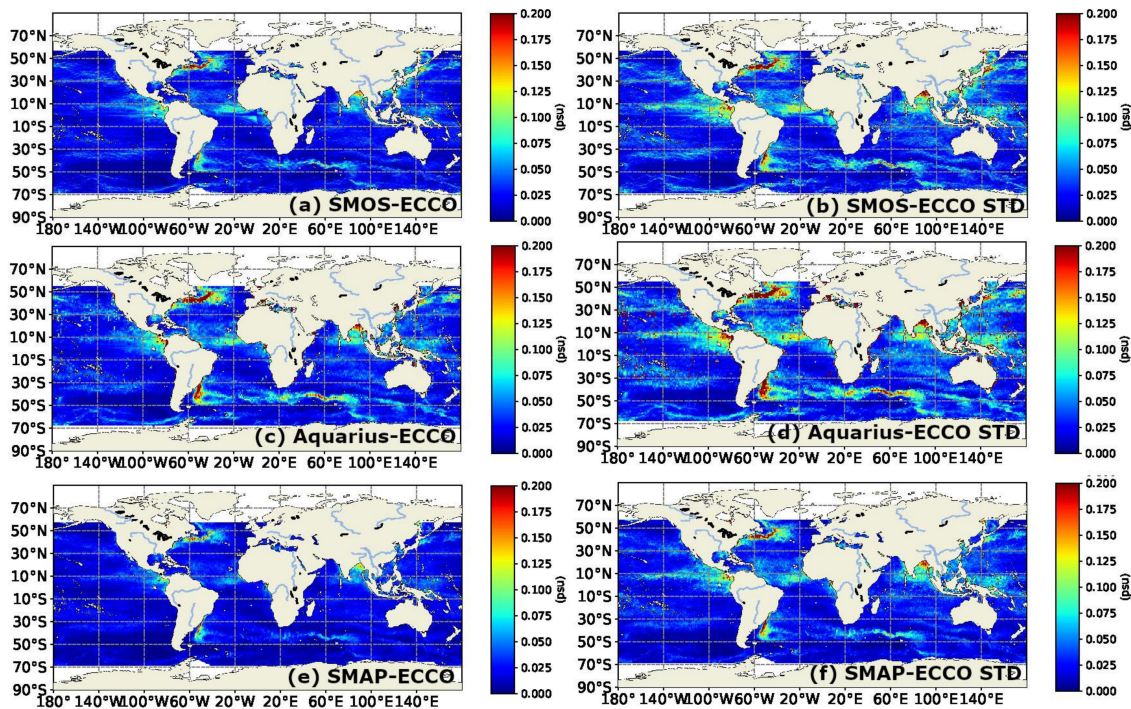
Figure 3. Maps of the absolute mean (**left column**) and standard deviation (**right column**) of differences between weekly (**a**,**b**) SMOS (9 days), (**c**,**d**) Aquarius (7 days), and (**e**,**f**) SMAP (8 days) and ECCO SSS over the 1-year model period.

From Figures 3a,c,e and 4a,c,e,g, we can see that the patterns of mean absolute differences between satellite and the model are similar from one product to the other with higher absolute values in a zone of high SSS variability (Figure 2). Indeed, in all products, regions such as the Gulf Stream, Kuroshio, Bay of Bengal, Pacific fresh pool, river mouths, or Antarctic Circumpolar Current (ACC) exhibit higher sampling error. However, the amplitude of the differences differs from one product to the other. While the differences between the simulated Argo-based product and model are particularly large (Figure 4g), the differences between the simulated SMAP and model data are lower (Figures 3e and 4e). Indeed, the differences between the simulated Argo-based product and model reach 1 psu at river mouths, in the Gulf Stream, and Pacific fresh pool at monthly time scales. On the other hand, the differences between simulated SMAP and model reach 0.2 (0.07) psu in the Gulf Stream and 0.15 (0.1) psu at river mouths, Pacific fresh pool, and in the Kuroshio at weekly (monthly) time scales.

We define the "sampling error" as the mean of the absolute difference between the ground truth model and the satellite or in situ product. Comparing the sampling errors from each satellite shows some discrepancies. SMAP exhibits on average the smallest sampling errors and sampling error variability both at weekly and monthly time scales (Figures 3e and 4e) globally, compared to SMOS and Aquarius (Figures 3a,c and 4a,c). Aquarius has larger sampling errors than both SMOS and SMAP in regions of high SSS variability. Indeed, the differences between simulated SMOS or Aquarius and the model

reach 0.5 (0.4) psu in the Gulf Stream and 0.2 (0.15) psu at river mouths, in the Kuroshio, and Pacific fresh pool at weekly (monthly) time scale.
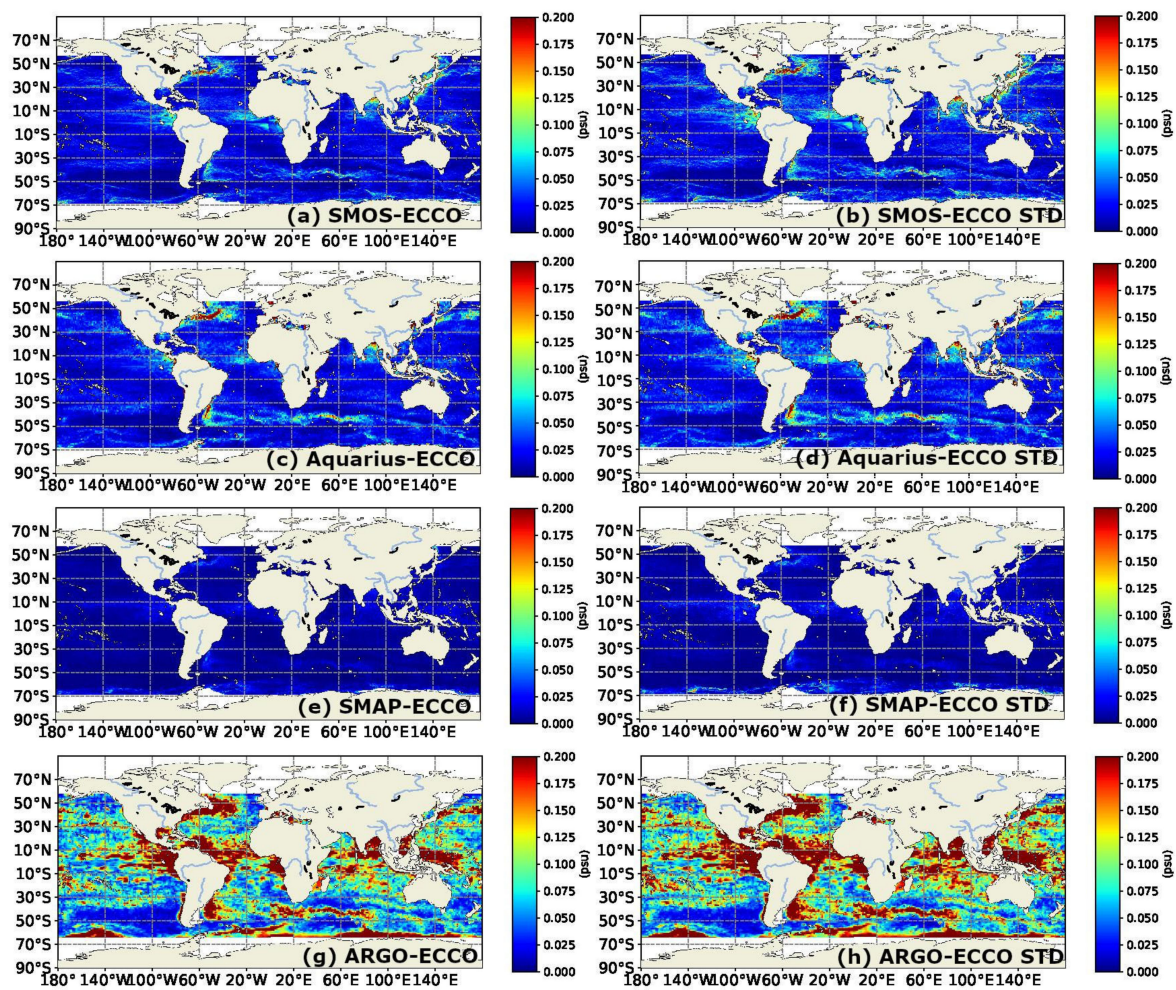

Figure 4. Maps of the absolute mean (**left column**) and standard deviation (**right column**) of differences between monthly (**a**,**b**) SMOS, (**c**,**d**) Aquarius, (**e**,**f**) SMAP, and (**g**,**h**) Argo-based and ECCO SSS over the 1-year model period.

Furthermore, regions of high standard deviations of these differences are similar within the four different datasets at weekly (Figure 3b,d,f) and monthly (Figure 4b,d,f,h) time scales. Indeed, regions with large SSS variability (see Figure 2) also tend to exhibit larger variability in the differences between satellite/in situ simulations and the model (i.e., larger sampling errors), reaching 0.5 psu for SMOS and Aquarius and 0.2 for SMAP in standard deviation at weekly and monthly time scales.

Comparing Figures 3 and 4, we see that the satellite sampling errors are larger at weekly than at monthly time scales as the variability (especially in regions of high variability (see Figure 2)) is smoothed over a month. Indeed, as mentioned above, the mean absolute differences and standard deviations of the differences reach higher values at weekly time scales than monthly time scales.

We now compare the global sampling error of each product. Figure 5 shows the histograms of the sampling error globally over the 1-year time period at weekly (when available) and monthly time scales, i.e., histograms of the fields depicted in Figures 3a,c,e and 4a,c,e,g. As pointed out earlier, the standard deviations of the distributions are larger at weekly time scales (from 0.026 (SMOS) to 0.435 (Aquarius) psu) than monthly time scales (from 0.015 (SMAP) to 0.205 (Aquarius) psu). The standard deviation of the weekly distributions of SMAP and Aquarius differences with ECCO are higher than that of SMOS

(Figure 5) as outliers impact the standard deviation values. While the range of the differences between SMOS and ECCO at weekly time scales is about 5.3 psu, the range of the differences between SMAP and ECCO reaches 9.5 psu and the range of the differences between Aquarius and ECCO reaches 11 psu. We thus decided to use the interquartile range (IQR) that is another way to measure the spread of values in a dataset [34]. However, unlike the standard deviation, the IQR is not affected by extreme outliers and is thus more appropriate in our case. The IQR of the weekly distribution of the differences between SMAP and ECCO is slightly lower than that of SMOS (0.016 psu versus 0.020 psu) and the IQR of the weekly distribution of the differences between Aquarius and ECCO is also similar, about 0.027 psu. Regarding the monthly distributions, the IQR for SMAP (0.006 psu) is lower than that of SMOS (0.029 psu) and of Aquarius (0.02 psu). Finally, the IQR of the difference between in situ and ECCO is about 0.09 psu, significantly higher than for all the satellite products.
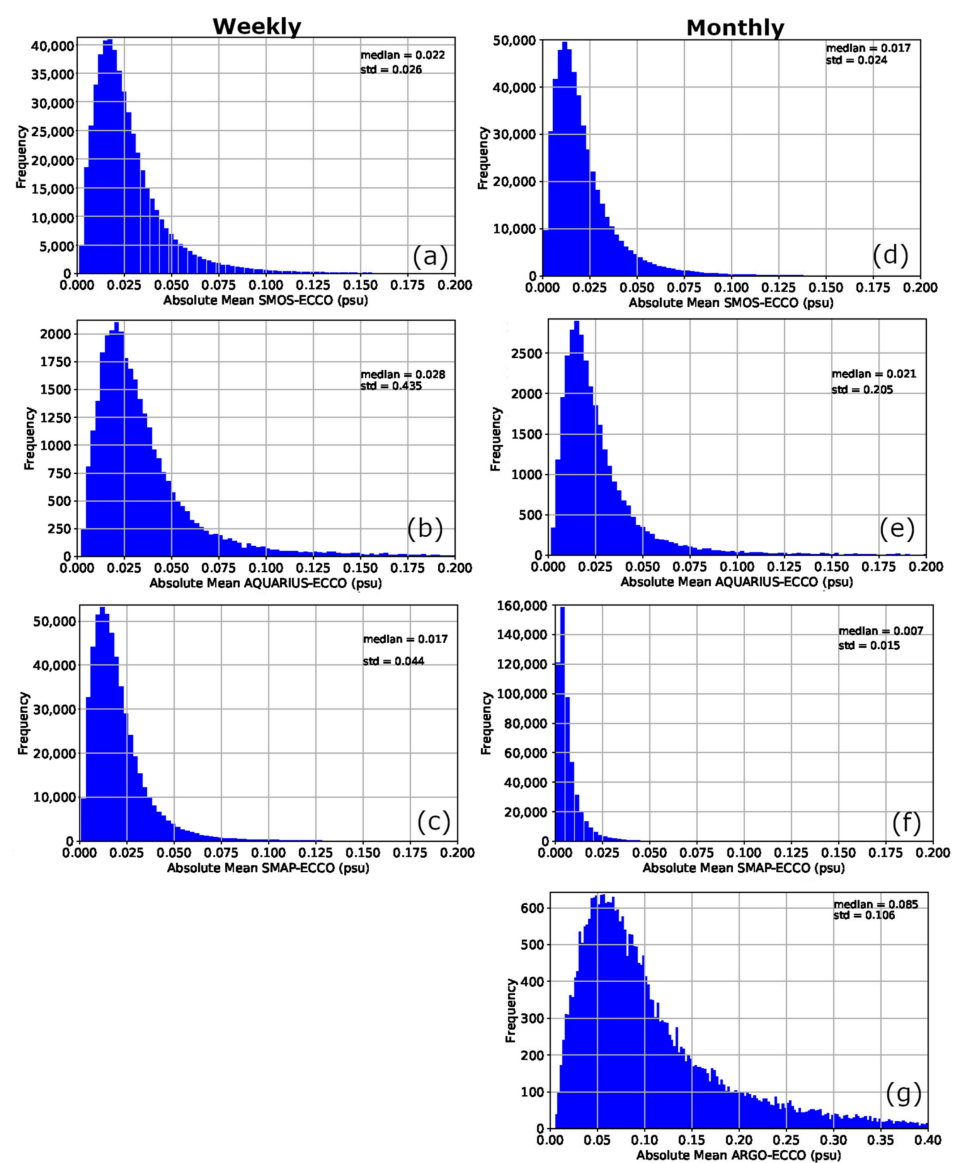
Figure 5. Histograms of the sampling error, i.e., the global absolute differences between our weekly ground truth (ECCO model) and (**a**) SMOS (9 days), (**b**) Aquarius (7 days), and (**c**) SMAP (8 days) SSS and between our monthly ground truth (ECCO model) and (**d**) SMOS, (**e**) Aquarius, (**f**) SMAP, and (**g**) ARGO. Note different x-axis limits for panel (**g**). Median (the global sampling error) and standard deviation of the sampling error is given in the upper right-hand corner of each panel.

We define the "global sampling error" as the median value of the sampling error at monthly and weekly time scales (Figure 5) over the globe. As mentioned earlier, the sampling errors are larger at weekly time scales (from 0.017 to 0.028 psu) than at monthly time scales (from 0.007 to 0.021 psu). At monthly time scales, the sampling error is higher for Aquarius (0.021 psu) than that of SMOS (0.017 psu) and SMAP (0.007 psu). Additionally, the sampling error is significantly higher for the in situ product (0.085 psu) than for satellite products (0.007 to 0.021 psu).

The simulated L3 satellite and in situ data we used came with no measurement error. However, real satellite and in situ observations include all the errors associated with the instrument, problems in the retrieval process, etc. [8,12]. While our study did not consider the measurement error, in the following, we want to see what the impact of adding noise to the data would have on our results. For that, we add a normally distributed noise with zero mean and a standard deviation of 0.1 to the L2 satellite values as was performed in [17]. Then, we recomputed the L3 grids at weekly and monthly time scales. Figure 6 is similar to Figure 5 with noise added to the satellite data. Now, the median of the absolute satellite-model differences at monthly time scales increases and ranges from 0.013 to 0.022 psu and from 0.024 to 0.032 psu at weekly time scales. This value is now impacted by a simulated measurement error and represents both the sampling error due to space and time misrepresentation and an estimated instrument/retrieval error.
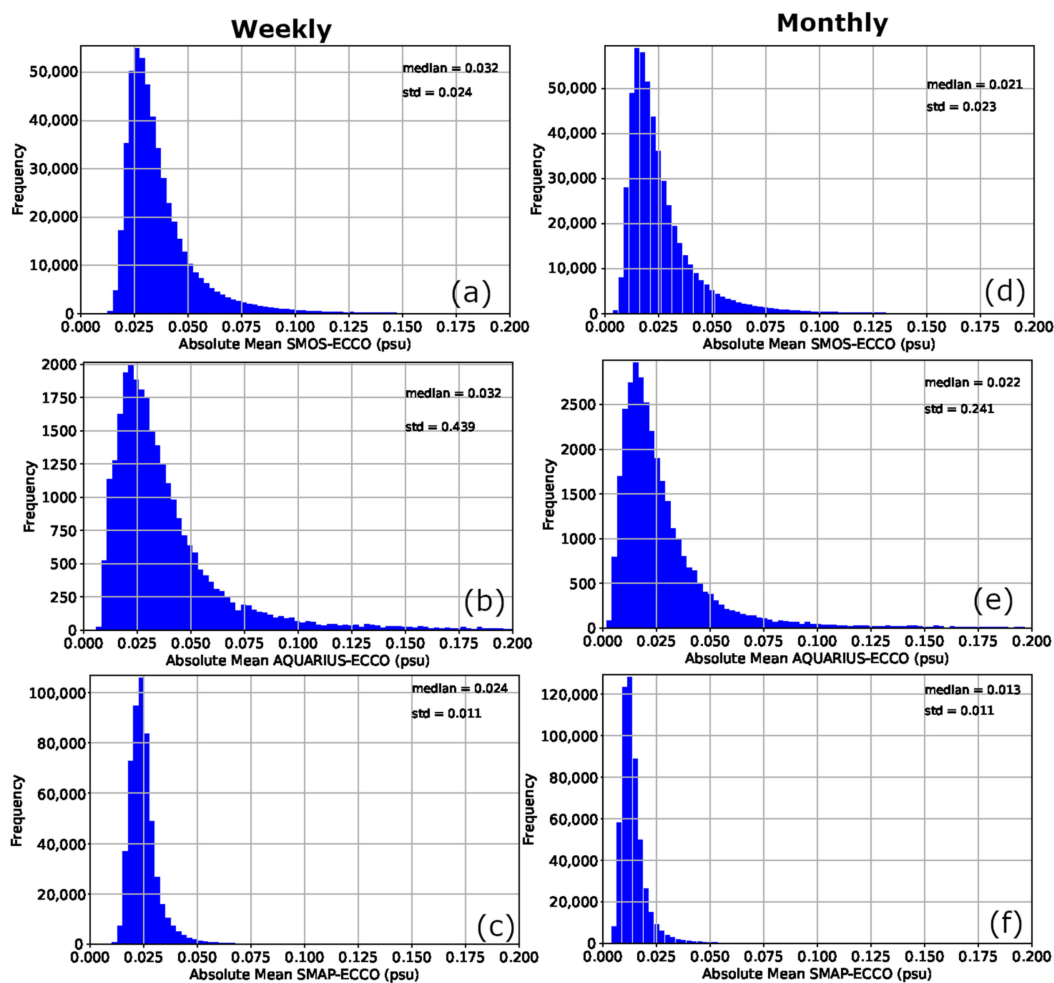
Figure 6. Histograms of the absolute differences between our monthly/weekly ground truth (ECCO model) and (**a**,**d**) SMOS, (**b**,**e**) Aquarius, and (**c**,**f**) SMAP SSS with a normally distributed noise with zero mean and a standard deviation of 0.1 added.

Alternatively, we have applied a recently developed formulation of the triple collocation method, the correlated triple collocation (CTC), as presented in [35], to characterize the standard deviation of the sampling error of each product. The CTC method is a new formulation of the triple collocation method that has been used to quantify several remote sensing SSS products [36,37]. Unlike the triple collocation method, the CTC methodology is intended for datasets of the same target defined at the same spatial scale, but for which the independence of the acquisition process cannot be assured (typically data from remote sensing platforms). Since the CTC method assumes all datasets are defined at the same spatial scale, we need to reduce the effective spatial resolution of SMAP and ECCO datasets to match that of the SMOS dataset. To do that, we have applied a gaussian filter with a 3×3 pixel kernel. Figure 7 shows the spectral analysis of the different SSS products. It shows that the ECCO (dark blue) and SMAP (dark green) non-filtered SSS products are resolving smaller scales than the SMOS product. After filtering, the ECCO and SMAP datasets are resolving the same temporal and spatial scales as SMOS (Figure 7). The CTC method was not applied to the Argo-based gridded and Aquarius datasets as they are not resolving the same temporal and spatial scales as SMAP and SMOS.
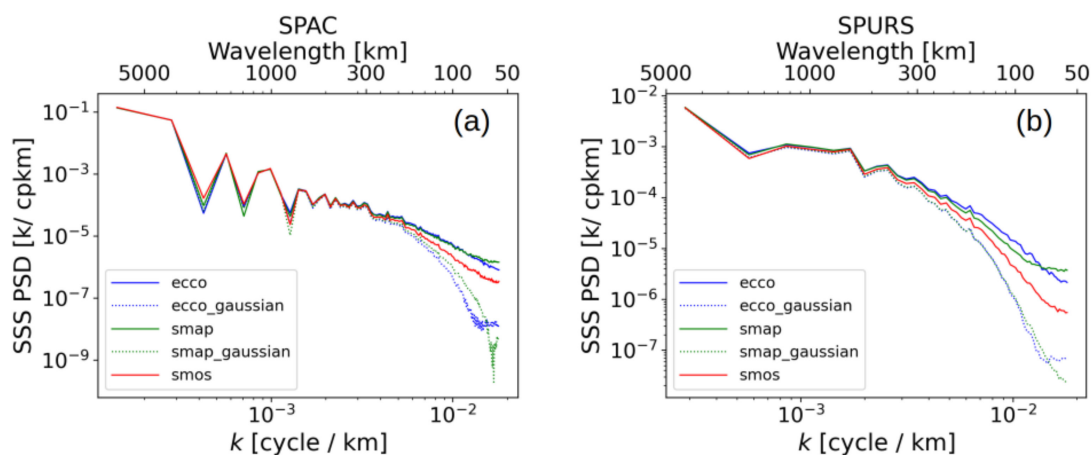
Figure 7. Spectral analysis of SSS from ECCO model (blue), simulated SMAP (green) and simulated SMOS (red) for two different regions (**a**) subtropical North Atlantic (SPURS) (22°N, 28°N; 60°W, 28°W) and (**b**) South Pacific (SPAC) (50°S, 14°N; 128°W, 112°W). Dashed lines correspond to the filtered SSS for ECCO (blue) and SMAP (green).

Figure 8 shows the results from the CTC analysis: the estimated error's standard deviations for the analyzed triplet: weekly simulated SMOS, simulated SMAP and ECCO. As expected, the estimated error's standard deviations are larger in the regions with higher salinity dynamics, such as the eastern boundaries currents, Bay of Bengal and the equatorial Atlantic which is affected by the Amazon River plume. The spatial patterns obtained are similar to those observed in Figure 3.

By construction, the standard deviation of the error of the reference, in our case, the ECCO dataset should be roughly close to zero. This is not the case in regions with higher salinity dynamics, as shown in Figure 8, where it can reach values up to 0.10–0.2 psu. This is due to the uncertainty of the estimation of the standard deviation of the error that can be 10% of the signal variance [35]. It could be reduced by enlarging the sample of the dataset.
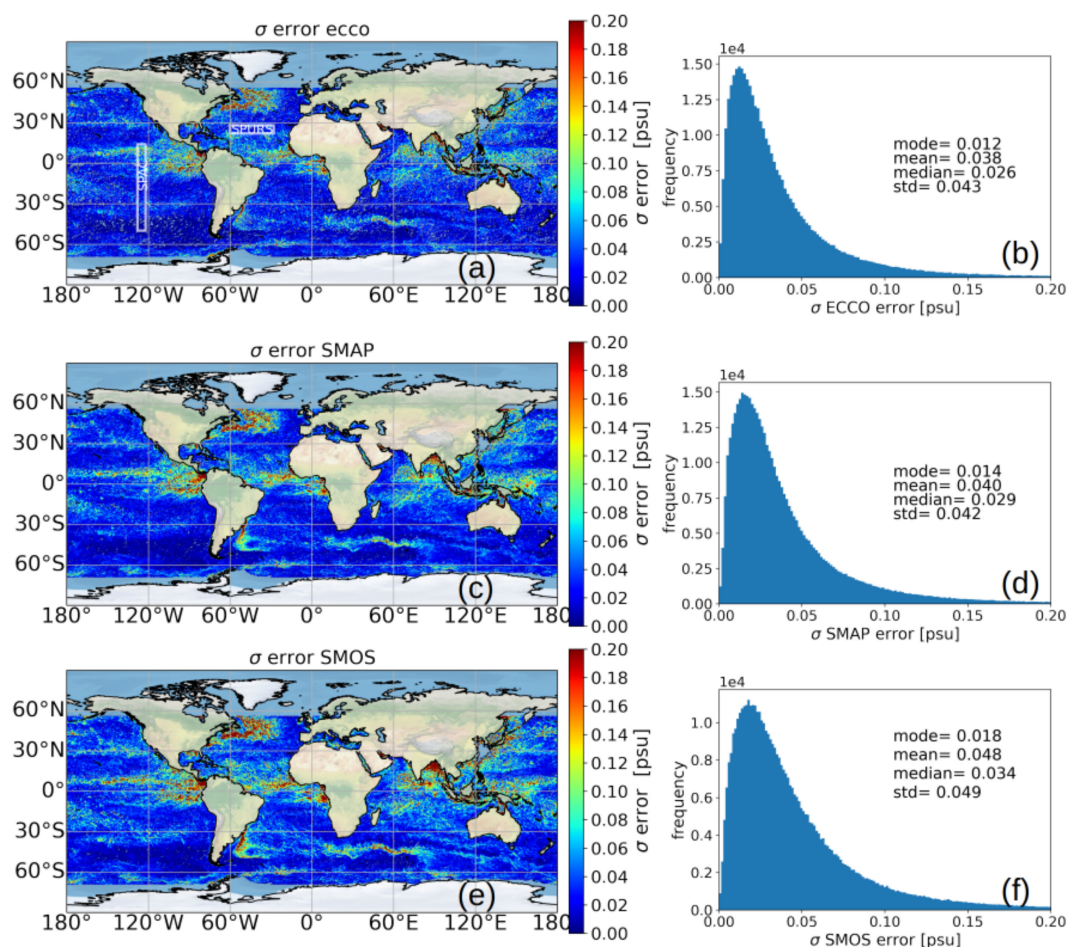
Figure 8. Maps of the error standard deviation (**left column**) and its associated histogram (**right column**) of the ecco model (**a,b**) simulated SSS satellite for SMAP (**c,d**) and SMOS (**e,f**). White solid lines in panel (**a**) delimit the regions considered to compute the spectral analysis of SSS shown in Figure 7.

4. Discussion

In Figures 3 and 4, we showed that the sampling errors are higher in regions of high SSS variability such as the Gulf Stream, Kuroshio, ACC, river plume regions, etc. This is consistent with findings from [5,16,19]. Indeed, these studies based on the (1/12°) HYCOM (Hybrid Coordinate Ocean Model) regridded onto a 1° grid, showed that sampling errors reach 0.7 psu in the Amazon River plume, 0.5 psu along the Gulf Stream, 0.4 psu in the Bay of Bengal, and above 1 psu in extreme cases. In the present study, we find that sampling errors can reach 0.15 (SMOS), 0.06 (SMAP) and 0.85 (Aquarius) psu in the Amazon River plume; 0.48 (SMOS), 0.50 (Aquarius), and 0.14 (SMAP) psu along the Gulf Stream; and 0.30 (SMOS), 0. 25 (Aquarius), and 0.11 (SMAP) psu in the Bay of Bengal. We should note that we did not use data from the first available pixel near the coast to make sure there was no residual land contamination. The Aquarius sampling errors found in our study are similar to the previous studies mentioned above in the three regions (as well as for SMOS in the Gulf Stream and Bay of Bengal regions). However, the SMAP sampling error in the Amazon River plume, Gulf Stream and Bay of Bengal are significantly smaller. One should keep in mind that river forcing is not well represented in the ECCO model as it is forced with climatological river data [38]. Therefore, sampling errors in river plume regions are underestimated.

This study is the first, to the authors' knowledge, to investigate the sampling error associated with an Argo-based gridded product. This is of major importance as [18] showed that sampling errors in gridded in situ products could have a large impact on the validation

process of satellite SSS products. Indeed, we showed that the sampling error associated with a commonly used Argo-based gridded product [10] is large and greater than the sampling errors of satellite products. This is probably due to the under-sampling in time and space of the ocean by single Argo floats, the nominal sampling of the Argo array being one profile per 3° latitude × 3° longitude at 10-day intervals, and less in marginal seas and coastal oceans where salinity variations have strong impacts on ocean dynamics, air–sea and ocean–ice interactions, and land–sea linkages [5]. This is especially important in coastal regions and other regions of high SSS variability. In [18], it is shown that the standard deviation of two commonly used Argo-based gridded products (including the one we reproduced in this study) is about 0.1 psu which is comparable to the standard deviation of the distribution of the sampling errors (differences between the Argo-based product simulated and the model) found in this study (0.1 psu in Figure 5). When no noise has been added to the data, the in situ-based product sampling error is still significantly higher than that of the three satellite products at monthly scales (0.085 psu). This stresses the need to be cautious when using in situ-based gridded products to validate satellite products.

The sampling errors of SMAP and SMOS computed earlier in this paper are consistent with the errors estimated by the CTC method presented in this paper. The sampling errors (~0.02 psu), their standard deviation (~0.04 psu) and their IQR (~0.02 psu) are similar to the SMOS and SMAP errors found using the CTC method. Table 1 summarizes all the statistics (sampling errors, standard deviation of the errors and IQR) for each product at weekly time scales and from the different methods. However, the SMOS and SMAP errors from the CTC method at the spatial scales resolved by the satellites, are similar to the ECCO (ground truth) error, indicating that the satellite sampling errors are small compared to the ground truth.

Table 1. Table summarizing the statistics of the methods to quantify each product's sampling error and standard deviation of the error, presented in this paper. The statistics here are for the weekly time scales for Aquarius, SMAP and SMOS. The CTC method was not applied on Aquarius as the method needs to be applied on datasets resolving the same spatial scales.

	First Analysis			
	Mean	**Median**	**Std**	**IQR**
SMAP-ECCO (psu)	0.022	0.017	0.044	0.016
SMOS-ECCO (psu)	0.028	0.022	0.026	0.020
Aquarius-ECCO (psu)	0.087	0.028	0.435	0.027
	CTC Analysis			
	mean	median	std	IQR
ECCO (psu)	0.038	0.026	0.043	0.033
SMAP (psu)	0.040	0.029	0.042	0.034
SMOS (psu)	0.048	0.034	0.049	0.041

5. Conclusions

In this study, we investigated for the first time the sampling errors associated with the three salinity satellites (SMOS, Aquarius and SMAP) and Argo-based in situ gridded products. By using a high-resolution model, we were able to do this without being impacted by measurement errors. We were able to simulate each satellite and in situ product on a high-resolution model and then to compute maps of the sampling errors associated with the Aquarius, SMAP, SMOS and in situ-based products at weekly (Figure 3) and monthly (Figure 4) time scales over our 1-year study period. We showed that the sampling errors are higher in regions of high SSS variability which is consistent with the findings from previous studies [5,16,19].

We also found that the sampling errors for SMOS and Aquarius are higher globally (0.022 and 0.028 psu, respectively, at weekly time scales and 0.017 and 0.021 psu, respectively, at monthly time scales) than that of SMAP at weekly and monthly time scales (0.017 and

0.007 psu, respectively). In addition, we found that the sampling errors associated with the in situ-based product are higher than that of the three satellite products at monthly scales (0.085 psu).

Another method to estimate errors of three datasets resolving similar spatial scales (SMAP, SMOS and ECCO) was used and gave similar results. This additional method showed that SMAP and SMOS sampling errors are similar to the ground truth sampling error (ECCO).

These findings are of extreme importance for the validation of satellite sea surface salinity products against in situ gridded products, as is commonly performed. Caution should be exercised when using in situ-based gridded products to validate or compare with satellite SSS products.

References

1. Font, J.; Camps, A.; Borges, A.; Martin-Neira, M.; Boutin, J.; Reul, N.; Kerr, Y.; Hahne, A.; Mecklenburg, S. SMOS: The challenging sea surface salinity measurement from space. *Proc. IEEE* **2010**, *98*, 649. [CrossRef]
2. Reul, N.; Chapron, B.; Lee, T.; Donlon, C.; Boutin, J.; Alory, G. Sea surface salinity structure of the meandering Gulf Stream revealed by SMOS sensor. *Geophys. Res. Lett.* **2014**, *41*, 3141–3148. [CrossRef]

3. Lagerloef, G.; DeCharon, A.; Lindstrom, E. Ocean Salinity and the Aquarius/SAC-D Mission: A New Frontier in Ocean Remote Sensing. *J. Mar. Technol. Soc.* **2013**, *47*, 26–30. [CrossRef]

4. Entekhabi, D.; Njoku, E.G.; O'Neill, P.E.; Kellogg, K.H.; Crow, W.T.; Edelstein, W.N.; Entin, J.K.; Goodman, S.D.; Jackson, T.J.; Johnson, J.; et al. The Soil Moisture Active Passive (SMAP) Mission. *Proc. IEEE* **2010**, *98*, 704–716. [CrossRef]

5. Vinogradova, N.; Lee, T.; Boutin, J.; Drushka, K.; Fournier, S.; Sabia, R.; Stammer, D.; Bayler, E.; Reul, N.; Gordon, A.; et al. Satellite Salinity Observing System: Recent Discoveries and the Way Forward. *Front. Mar. Sci.* **2019**, *6*, 243. [CrossRef]

6. Melnichenko, O.; Hacker, P.; Maximenko, N.; Lagerloef, G.; Potemra, J. Optimum interpolation analysis of Aquarius Sea surface salinity. *J. Geophys. Res. Ocean.* **2016**, *121*, 602–616. [CrossRef]

7. Boutin, J.; Reul, N.; Koehler, J.; Martin, A.; Catany, R.; Guimbard, S.; Rouffi, F.; Vergely, J.L.; Arias, M.; Chakroun, M.; et al. Satellite-Based Sea Surface Salinity Designed for Ocean and Climate Studies. *J. Geophys. Res. Ocean.* **2021**, *126*, e2021JC017676. [CrossRef]

8. Olmedo, E.; González-Haro, C.; Hoareau, N.; Umbert, M.; González-Gambau, V.; Martínez, J.; Gabarró, C.; Turiel, A. Nine years of SMOS sea surface salinity global maps at the Barcelona Expert Center. *Earth Syst. Sci. Data* **2021**, *13*, 857–888. [CrossRef]

9. Meissner, T.; Wentz, F.J.; Manaster, A.; Lindsley, R. *Remote Sensing Sytems SMAP Ocean Surface Salinities, Version 4.0*; Validated Release; Remote Sensing Systems: Santa Rosa, CA, USA, 2019. [CrossRef]

10. Roemmich, D.; Gilson, J. The 2004–2008 mean and annual cycle of temperature, salinity, and steric height in the global ocean from the Argo Program. *Prog. Oceanogr.* **2009**, *82*, 81–100. [CrossRef]

11. Good, S.A.; Martin, M.J.; Rayner, N.A. EN4: Quality controlled ocean temperature and salinity profiles and monthly objective analyses with uncertainty estimates. *J. Geophys. Res. Ocean.* **2013**, *118*, 6704–6716. [CrossRef]

12. Meissner, T.; Wentz, F.J.; Le Vine, D.M. The salinity retrieval algorithms for the NASA Aquarius Version 5 and SMAP Version 3 releases. *Remote Sens.* **2018**, *10*, 1121. [CrossRef]

13. Lagerloef, G.; Colomb, F.R.; Le Vine, D.; Wentz, F.; Yueh, S.; Ruf, C.; Lilly, J.; Gunn, J.; Chao, Y.; Decharon, A.; et al. The Aquarius/SAC-D mission: Designed to meet the salinity remote- sensing challenge. *Oceanography* **2008**, *21*, 68–81. [CrossRef]

14. Bingham, F.M. Subfootprint variability of sea surface salinity observed during the SPURS-1 and SPURS-2 field campaigns. *Remote Sens.* **2019**, *11*, 2689. [CrossRef]

15. Boutin, J.; Chao, Y.; Asher, W.E.; Delcroix, T.; Drucker, R.; Drushka, K.; Kolodziejczyk, N.; Lee, T.; Reul, N.; Reverdin, G.; et al. Satellite and in situ salinity: Understanding near-surface stratification and subfootprint variability. *Bull. Am. Meteorol. Soc.* **2016**, *97*, 1391–1407. [CrossRef]

16. Vinogradova, N.T.; Ponte, R.M. Small-scale variability in sea surface salinity and implications for satellite-derived measurements. *J. Atmos. Oceanic Tech.* **2013**, *30*, 2689–2694. [CrossRef]

17. Bingham, F.M.; Fournier, S.; Brodnitz, S.; Ulfsax, K.; Zhang, H. Matchup Characteristics of Sea Surface Salinity Using a High-Resolution Ocean Model. *Remote Sens.* **2021**, *13*, 2995. [CrossRef]

18. Lee, T. Consistency of Aquarius sea surface salinity with Argo products on various spatial and temporal scales. *Geophys. Res. Lett.* **2016**, *43*, 3857–3864. [CrossRef]

19. Vinogradova, N.T.; Ponte, R.M.; Fukumori, I.; Wang, O. Estimating satellite salinity errors for assimilation of Aquarius and SMOS data into climate models. *J. Geophys. Res. Ocean.* **2014**, *119*, 4732–4744. [CrossRef]

20. Delcroix, T.; McPhaden, M.J.; Dessier, A.; Gouriou, Y. Time and space scales for sea surface salinity in the tropical oceans. *Deep. Sea Res. Part I* **2005**, *52*, 787–813. [CrossRef]

21. Vinogradova, N.T.; Ponte, R.M. Assessing temporal aliasing in satellite-based salinity measurements. *J. Atmos. Oceanic Tech.* **2012**, *29*, 1391–1400. [CrossRef]

22. Meissner, T.; Wentz, F.; Manaster, A.; Lindsey, R. NASA/RSS SMAP Salinity: Version 4.0 Validated Release, Algorithm Theoretical Basis Document (ATBD). *Remote Sens. Syst. Tech. Rep.* **2019**, *82219*, 55. Available online: https://data.remss.com/smap/SSS/Release_V4.0.pdf (accessed on 1 March 2020).

23. Marshall, J.; Adcroft, A.; Hill, C.; Perelman, L.; Heisey, C. A finite-volume, incompressible Navier Stokes model for studies of the ocean on parallel computers. *J. Geophys. Res. Ocean.* **1997**, *102*, 5753–5766. [CrossRef]

24. Forget, G.; Campin, J.-M.; Heimbach, P.; Hill, C.N.; Ponte, R.M.; Wunsch, C. ECCO version 4: An integrated framework for non-linear inverse modeling and global ocean state estimation. *Geosci. Model Dev.* **2015**, *8*, 3071–3104. [CrossRef]

25. Rocha, C.B.; Gille, S.T.; Chereskin, T.K.; Menemenlis, D. Seasonality of submesoscale dynamics in the kuroshio extension. *Geophys. Res. Lett.* **2016**, *43*, 11304–11311. [CrossRef]

26. Wang, J.; Fu, L.-L.; Qiu, B.; Menemenlis, D.; Farrar, J.; Chao, Y.; Thompson, A.F.; Flexas, M.M.; Farrar, T. An observing system simulation experiment for the calibration and validation of the surface water ocean topography sea surface height measurement using in situ platforms. *J. Atmos. Ocean. Technol.* **2018**, *35*, 281–297. [CrossRef]

27. Qiu, B.; Chen, S.; Klein, P.; Wang, J.; Torres, H.; Fu, L.-L.; Menemenlis, D. Seasonality in transition scale from balanced to unbalanced motions in the world ocean. *J. Phys. Oceanogr.* **2018**, *48*, 591–605. [CrossRef]

28. Savage, A.C.; Arbic, B.K.; Alford, M.H.; Ansong, J.K.; Farrar, J.T.; Menemenlis, D.; O'Rourke, A.K.; Richman, J.G.; Shriver, J.F.; Voet, G.; et al. Spectral decomposition of internal gravity wave sea surface height in global models. *J. Geophys. Res. Ocean.* **2017**, *122*, 7803–7821. [CrossRef]

29. Su, Z.; Wang, J.; Klein, P.; Thompson, A.F.; Menemenlis, D. Ocean submesoscales as a key component of the global heat budget. *Nat. Commun.* **2018**, *9*, 775. [CrossRef]

30. Arbic, B.K.; Alford, M.H.; Ansong, J.K.; Buijsman, M.C.; Ciotti, R.B.; Farrar, J.T.; Hallberg, R.W.; Henze, C.E.; Hill, C.N.; Luecke, C.A.; et al. Primer on Global Internal Tide and Internal Gravity Wave Continuum Modeling in HYCOM and MITgcm. In *New Frontiers in Operational Oceanography*; Chassignet, E., Pascual, A., Tintoré, J., Verron, J., Eds.; GODAE OceanView: Tallahassee, FL, USA, 2018; pp. 307–392. [CrossRef]

31. Camps, A.; Corbella, I.; Bara, J.; Torres, F. Radiometric sensitivity computation in aperture synthesis interferometric radiometry. *IEEE Trans. Geosci. Remote Sens.* **1998**, *36*, 680–685. [CrossRef]

32. Kuusela, M.; Stein, M.L. Locally stationary spatio-temporal interpolation of Argo profiling float data. *Proc. R. Soc. A* **2018**, *474*, 20180400. [CrossRef]

33. Park, B.; Kuusela, M.; Giglio, D.; Gray, A. Spatio-Temporal Local Interpolation of Global Ocean Heat Transport Using Argo Floats: A Debiased Latent Gaussian Process Approach. *Ann. Appl. Stat. arXiv* **2022**, arXiv:2105.09707. [CrossRef]

34. Dekking, F.M.; Kraaikamp, C.; Lopuhaä, H.P.; Meester, L.E. *A Modern Introduction to Probability and Statistics: Understanding Why and How*; Springer: London, UK, 2005; Volume 488, ISBN 978-1-85233-896-1. [CrossRef]

35. González-Gambau, V.; Turiel, A.; González-Haro, C.; Martínez, J.; Olmedo, E.; Oliva, R.; Martín-Neira, M. Triple collocation analysis for two error-correlated datasets: Application to l-band brightness temperatures over land. *Remote Sens.* **2020**, *12*, 3381. [CrossRef]

36. Hoareau, N.; Portabella, M.; Lin, W.; Ballabrera-Poy, J.; Turiel, A. Error characterization of sea surface salinity products using triple collocation analysis. *IEEE Trans. Geosci. Remote Sens.* **2018**, *56*, 5160–5168. [CrossRef]

37. Ratheesh, S.; Mankad, B.; Basu, S.; Kumar, R.; Sharma, R. Assessment of satellite-derived sea surface salinity in the Indian Ocean. *IEEE Geosci. Remote Sens. Lett.* **2012**, *10*, 428–431. [CrossRef]

38. Menemenlis, D.; Campin, J.M.; Heimbach, P.; Hill, C.; Lee, T.; Nguyen, A.; Schodlok, M.; Zhang, H. ECCO2: High resolution global ocean and sea ice data synthesis. *Mercator Ocean. Q. Newsl.* **2008**, *31*, 13–21.

39. Argo. *Argo Float Data and Metadata from Global Data Assembly Centre (Argo GDAC)*; Seanoe: Plouzané, France, 2021. [CrossRef]